

High resolution x-ray diffraction microscopy of specifically labeled yeast cells

Johanna Nelson¹, Xiaojing Huang¹, Jan Steinbrener¹, David Shapiro², Janos Kirz², Stefano Marchesini², Aaron M. Neiman³, Joshua J. Turner¹, Chris Jacobsen¹

The classification is Physical Sciences with the subcategory Physics. The text (including references and figure legends) spans five pages with a total of 4 figures. The following abbreviations are used XDM for x-ray diffraction microscopy, YPD for yeast peptone dextrose, CCD for charge-coupled device, (S)TXM for (scanning) transmission x-ray microscope, and SEM for scanning electron microscope.

Correspondence should be directed to the first author

Johanna Nelson
Dept. Physics & Astronomy
Stony Brook University
Stony Brook, NY 11794-3800, USA
Johanna.Nelson@stonybrook.edu
phone: (631) 632-8002
fax: (631) 632- 8101

¹Dept. Physics and Astronomy, Stony Brook University, Stony Brook, NY 11794-3800

²Advanced Light Source, Lawrence Berkeley National Laboratory, Berkeley, CA 94720

³Dept. Biochemistry and Cell Biology, Stony Brook University, Stony Brook, NY 11794-5215

High resolution x-ray diffraction microscopy of specifically labeled yeast cells

Johanna Nelson ^{*}, Xiaojing Huang ^{*}, Jan Steinbrener ^{*}, David Shapiro [†], Janos Kirz [†], Stefano Marchesini [†], Aaron M. Neiman [‡], Joshua J. Turner ^{*}, Chris Jacobsen ^{*},

^{*}Dept. Physics and Astronomy, Stony Brook University, Stony Brook, NY 11794-3800, [†]Advanced Light Source, Lawrence Berkeley National Laboratory, Berkeley, CA 94720, and [‡]Dept. Biochemistry and Cell Biology, Stony Brook University, Stony Brook, NY 11794-5215

Submitted to Proceedings of the National Academy of Sciences of the United States of America

X-ray diffraction microscopy complements other x-ray microscopy methods by being free of lens-imposed radiation dose and resolution limits, and it allows for high resolution imaging of biological specimens too thick to be viewed by electron microscopy. We report here the highest resolution (11–13 nm) x-ray diffraction micrograph of biological specimens, and the first demonstration of molecular-specific gold labeling at different depths within cells via through-focus propagation of the reconstructed wavefield. The lectin concanavalin A conjugated to colloidal gold particles was used to label the α -mannan sugar in the cell wall of the yeast *Saccharomyces cerevisiae*. Cells were plunge-frozen in liquid ethane and freeze-dried after which they were imaged whole using x-ray diffraction microscopy at 750 eV photon energy.

x-ray microscopy | coherent imaging | immunogold labeling

Abbreviations: XDM, x-ray diffraction microscopy; YPD, yeast peptone dextrose; CCD, charge-coupled device; (S)TXM, (scanning) transmission x-ray microscope; SEM, scanning electron microscope

Introduction

X-ray microscopes can be used for the imaging of unsectioned eukaryotic cells too thick to be viewed in their entirety using electron microscopy (1–3), with the potential for higher spatial resolution than even the most advanced optical microscopy methods (see *e.g.* (4)). These advantages are being realized in a number of ways, such as the imaging of trace metals and metalloproteins with improved detection limits (5,6), and tomographic imaging of frozen hydrated cells at 40–60 nm resolution (7–11). Such efforts are leading to the availability of x-ray microscopes at most synchrotron radiation research centers, and laboratory-based systems are also beginning to appear (12,13).

Although most lens-based x-ray imaging of biological specimens has been done at 40–60 nm resolution range, the spatial resolution of x-ray microscopes has been steadily improving (?), with demonstrations in specific test cases of optics with resolutions around 15 nm (15–17). Even so, practical challenges remain in lens-based x-ray imaging. Soft x-ray Fresnel zone plates with outermost zone widths smaller than 20 nm have had sub-millimeter short focal lengths as well as focusing efficiencies well below 10%. The former creates geometric complications for tomographic imaging while the latter translates to an increase in radiation damage to the specimen when zone plates are used in transmission x-ray microscope (TXM) systems. To reduce the damage from radiation, biological materials have been successfully imaged with x-rays in the frozen hydrated state with no artifact-causing pre-treatment (18,19). For hydrated specimens, both phase and amplitude contrast are maximized when working in the “water window”, the spectral region between the carbon and oxygen *K*-shell energies (18,20). However at a “water window” energy of 540 eV and a spatial resolution of 20 nm, the depth of focus of a standard monochromatic zone plate imaging system approaches the half micrometer thickness at which

cryo electron tomography at 5–6 nm resolution becomes possible (2,21). As a result, while progress is ongoing in lens-based x-ray imaging, it is also valuable to consider alternative approaches to high-resolution x-ray imaging of thick biological specimens with minimum radiation exposure.

X-ray diffraction microscopy (XDM; also known as coherent x-ray diffraction imaging) provides one such alternative approach. By illuminating an isolated specimen with a coherent beam and recording the far-field diffraction intensities, one can reconstruct the complex wavefield leaving the object (22). This approach was first proposed as a method for x-ray microscopy by Sayre (23), and was first demonstrated in 1999 by Miao *et al.* (24). Because there is no lens between the specimen and the detector, XDM does not suffer from the resolution limits of the lens nor its efficiency losses, so that in principle higher resolution images can be obtained for a given specimen exposure (25). Furthermore, by recording a series of diffraction patterns as the specimen is rotated through a large tilt range, one can obtain a complex, 3D image (26,27) and projection images free of depth of focus limitations (27). In fact, considerations of radiation damage suggest that the method can be used for 10-nm resolution 3D imaging of whole, frozen hydrated cells (28,29). At present, published work of XDM on biological specimens has been done at room temperature on dehydrated specimens, though efforts are underway to image frozen hydrated specimens (30,31). Prior work includes the imaging of non-specifically-stained bacteria (32), a yeast cell (33), sections of intramuscular fish bone (34), a single virion (35), malaria-infected erythrocytes imaged using a Fresnel version of the technique (36), and a human chromosome imaged in 3D (37). Although most published resolutions are better than those typically seen in lens-based imaging of biological specimens, none have resolutions finer than 22 nm.

Here we report a resolution between 11–13 nm, the highest resolution in x-ray imaging of a biological specimen. It is also the first use of molecule-specific labeling in XDM. Resolving labels in 3D is important for building up a view of the function of the specific molecule or organelle that is tagged. By moving the focus through the specimen, we are able to identify the depth of labels with a precision of 130 nm. We also apply this technique to focus on a specific label and use the

Reserved for Publication Footnotes

size of this high contrast feature as an independent measure of resolution.

Results

In Fig. 1, we show the reconstructed XDM image of a pair of yeast cells along with images acquired later of the same specimen using a scanning transmission x-ray microscope (STXM) at beamline 11.0.2 at the Advanced Light Source (using a Fresnel zone plate with 25 nm outermost zone width and a theoretical Rayleigh resolution of 30 nm) and a Zeiss LEO 1550 SFEG scanning electron microscope (SEM). Correlative microscopy provides strong confirmation of the fidelity of the XDM image, and allows for greater confidence in the proposed identification of subcellular components (nucleus, vacuole, mitochondrion) and surface labeling as noted in the figure. In addition, since in XDM one reconstructs a complex wavefield corresponding to the focal plane where the object boundaries best agree with the support (such as the mid-plane for a spherical cell (38, 39)), this plane can be shifted forward or backward by convolution with a Fresnel propagation kernel. In Fig. 1, panels b and c show the reconstructed wavefield propagated to the front and back surfaces of the cells (see Supplementary Movie S1 for a video of the propagation); these views agree well with the SEM micrographs shown in panels e and f obtained by manually flipping the sample. For high-contrast, isolated gold labels, the presence or absence of near-field defocus fringes can be used to identify the longitudinal position of particular isolated labels in the XDM reconstruction; these positions correlate well with the “front” and “back” side of the cells as seen in the SEM images. This can be seen despite the geometrical distortion provided by different sample tilts in the SEM, and by the different appearance of larger features in the SEM image versus in the XDM reconstruction (where the contrast of larger features is compromised due to the missing data obscured by the detector beamstop).

The silver-enhanced gold labels serve as good reference structures for estimating the spatial resolution of the reconstructed image. In Fig. 2, we show a magnitude image at right where the region containing the label is shown with the 10.6 nm pixels enlarged. At left the region is shown in a cubic interpolated representation with 0.53 nm pixels with an overlay of isomagnitude contour lines, where yellower hue indicates larger magnitude. The interpolated representation was then fit to a two dimensional Gaussian function so as to avoid a possible bias in the resolution estimation due to the choice of a particular single line profile through the object. The resulting fit, shown in Fig. 2, involves a Gaussian with a full-width at half maximum (FWHM) minor diameter of 44.8 nm and a major diameter of 51.2 nm. The SEM image of Fig. 1 was used to find that this silver-enhanced gold label has a radius of $31.9 \text{ nm} \pm 2.5 \text{ nm}$. Convolution of the thickness function of a sphere of this radius with Gaussian point spread functions of varying widths suggests a resolution of the XDM exitwave in the range of 11 to 20 nm (see Supplementary Figure S2).

A second estimate of the spatial resolution is provided by the phase retrieval transfer function (PRTF) (27), which is defined as the spatial-frequency-dependent ratio of the magnitudes of the averaged reconstructed wavefield divided by the experimentally recorded diffraction magnitudes. Since the averaging procedures described in Materials and Methods lead to reproducible Fourier amplitudes being reinforced while non-reproducible amplitudes approach an average of zero, the spatial frequency at which this metric decays sharply tells about the length scale at which reliable phasing declines. As shown in Fig. 3, the PRTF for the reconstructed image begins to

show a decline at a half-period resolution around 12.5 nm. At the spatial frequency corresponding to the real space pixels size of 10.6 nm, the PRTF value has dropped below 0.5, suggesting a half-period spatial resolution in the 11–13 nm range. This is consistent with the bounds given by the Gaussian resolution estimation obtained from Fig. 2 and is the finest resolution reported to date in XDM of an organic specimen. While higher spatial resolution has been described in non-biological XDM studies (41), our estimate is based on both internal structure rather than edge sharpness (which can be affected by the imposition of a tight finite support constraint), and on a higher value of the PRTF (around 0.5 versus 0.1).

As noted above, XDM can be used for 3D imaging by acquiring a tilt series of diffraction patterns and performing a 3D iterative reconstruction (26, 27), including on biological specimens (37). For the gold-labeled yeast specimen studied here, the lack of protection from cryogenic cooling meant that radiation limited the number of tilt angles over which diffraction data could be collected (too few for a 3D iterative reconstruction or a tomographic reconstruction of XDM projections). Figure 4 shows the complex exit waves for specimen tilts of -30° and $+15^\circ$ obtained using the same 2D reconstruction procedure as described above for the 0° data. Consistencies between these separately reconstructed angles give confidence to the identification of specific organelles.

Discussion

The work reported here represents a first demonstration that the high spatial resolution of XDM can be used for molecule-specific imaging using gold labeling. By propagating the exitwave, labels in different focal planes can be brought into focus thereby overcoming the limited depth of focus of the 2D projection. An alternative approach to extracting the 3D information from a 2D diffraction pattern, which has recently shown promising results on sparse objects (42), was not attempted on this non-sparse sample. While the results reported here are of a dehydrated specimen viewed in 2D at room temperature, several groups (including our own) are now working towards 3D XDM studies using frozen hydrated specimens. These efforts complement the immediate viewing capabilities of optic-based x-ray microscopes, and the combination of optic-based microscopy with coherent diffraction approaches (43, 44) may allow both to be achieved in one experiment.

Materials and Methods

We imaged the *whi5* mutant (45) of *Saccharomyces cerevisiae*, which produces smaller (3–4 μm diameter) yeast cells than the 6–7 μm diameter typical of the wild type. To label the α -mannan sugars found in the cell walls of the yeast (46), we used the mannose binding protein concanavalin A (conA) conjugated to 1.8 nm gold particles from Nanoprobes Incorporated (Yaphank, NY). Cells were cultured in YPD medium at 30°C , rinsed, and then placed in suspension, without fixation, in a dilute solution of the conA-gold resulting in a random distribution of gold particles across the surface of the cell. A light-sensitive silver enhancer from Nanoprobes Incorporated (Yaphank, NY) was then used to increase the size of the labels. After labeling and enhancement, the cells were diluted with distilled water to the proper concentration and then allowed to settle on a formvar-coated, carbon stabilized electron microscopy grid before being plunge frozen in liquid ethane to minimize ice crystal formation. An EMS775X turbo freeze-drier from Electron Microscopy Sciences (Hatfield, PA) was used to dry the frozen specimens by sublimation, thereby

avoiding both ice re-crystallization and cell collapse that could otherwise result from air drying.

Following specimen preparation, coherent x-ray diffraction data were recorded at 750 eV photon energy using an experimental apparatus developed at Stony Brook (47) and located at beamline 9.0.1 of the Advanced Light Source at Lawrence Berkeley National Laboratory. Our procedure was similar to what we have previously reported for imaging yeast cells (33). The required spatial and temporal coherence were achieved using a 5 μm pinhole located 25 mm upstream of the specimen. By employing a moveable beamstop and recording multiple summed exposures, we were able to record diffraction data over a range of scattering angles and intensities on a Roper Scientific (Trenton, NJ) MTE-2 CCD detector with 1340×1300 pixels of 20 μm size, located 13 cm downstream from the specimen. At each tilt angle, a total of 34 diffraction patterns were taken at different beamstop positions and exposure times; the total x-ray exposure time was 406.2 seconds with an estimated cumulative irradiance of 1.7×10^9 photons/ μm^2 ; this corresponds to an estimated skin dose to $\rho = 1.35 \text{ g/cm}^3$ dense protein of 1.2×10^8 Gray. The individual exposures were combined using a newly-developed automated assembly program (Steinbrener *et al.*; manuscript in preparation) to obtain a single diffraction intensity image. The final image had a dynamic range of over five orders of magnitude and a 19×19 missing pixel region in the centre due to the saturation limits of the detector.

From the full assembled array, a 1024×1024 subset was used for the image reconstruction process, with a maximum spatial frequency of 67 μm^{-1} or 7.5 nm half-period at the corners, and a real space pixel size of 10.6 nm. An initial approximation of the object's support (the reconstruction array subspace within which the specimen is constrained to fit (22)) was obtained from the autocorrelation of the diffraction pattern; it was subsequently tightened using a combination of the shrinkwrap algorithm (48) and manual adjustment. For iterative reconstructions, we used the difference map algorithm (39,49) with a positivity constraint applied to the imaginary part of the complex array (effectively limiting the maximum phase shift through the specimen to π , corresponding to

a total projected thickness limit of 1.5 μm of solid dry protein). A total of ten independent iteration runs were performed using the same tightened object support. For each of the ten runs, we began with a random initial phase start and ran for 2,000 iterations. At this point, we carried out another 8,000 iterations where the complex Fourier projection was saved every 100 iterations for averaging at the end (thereby reinforcing consistent phase while averaging out fluctuations (39)). Before results were averaged the global phase was adjusted to a common value using the method suggested by Chapman *et al.* (27). At the end of these separate procedures of 10,000 iterations each, the ten resulting averaged reconstructions had any remaining linear phase ramps removed, were high-pass filtered to reduce the signal from the unconstrained low spatial frequencies corresponding to the missing pixels region, and their global phases were reset such that the real part of the complex array was maximized (39) before being averaged together to yield the final complex image. Finally, to compare the complex reconstructed wavefield to the transmission x-ray micrograph, we multiplied the wavefield by a constant phase and added an amplitude such that the scatterplot of the wavefield begins in the positive real and imaginary quadrant and spirals toward negative values. Due to Babinet's principle (50), such uniform adjustments are valid since they are only detectable in the low-spatial frequency signal blocked by our beamstop.

ACKNOWLEDGMENTS. We would like to thank the National Institute for General Medical Services at the National Institutes for Health for its support of the application of XDM to biological imaging under contract 5R21EB6134. We thank the Division of Materials Sciences and Engineering, Office of Basic Energy Sciences, at the Department of Energy for support of XDM methods and instrumentation development under contract DE-FG02-07ER46128. We also want to extend our appreciation to David Sayre and Malcolm Howells for their continued contribution. We wish to thank Vishwas Joshi of Nanoprobes Incorporated for the custom-made labels and silver enhancement kit and Stefan Vogt at the Advanced Photon Source for his help with specimen freeze-drying. We would also like to thank Jim Quinn at Stony Brook University for help with the SEM images. Finally, we wish to thank the Advanced Light Source staff for their support, especially Tolek Tyliczszak, beamline scientist at beamline 11.0.2 for his help with the STXM image. The Advanced Light Source is supported by the Director, Office of Science, Office of Basic Energy Sciences, of the U.S. Department of Energy under contract DE-AC02-05CH11231.

- Sayre, D, Kirz, J, Feder, R, Kim, DM, Spiller, E (1977) Potential operating region for ultrasoft x-ray microscopy of biological specimens. *Science* 196:1339–1340.
- Grimm, R et al. (1997) Energy filtered electron tomography of ice-embedded actin and vesicles. *Biophysical Journal* 72:482–489.
- Jacobsen, C, Medenwaldt, R, Williams, S (1998) A perspective on biological x-ray and electron microscopy eds Thieme, J, Schmahl, G, Umbach, E, Rudolph, D (Springer-Verlag, Berlin), pp 11–93–102.
- Hell, S (2007) Far-field optical nanoscopy. *Science* 316:1153–1158.
- Paunesku, T, Vogt, S, Maser, J, Lai, B, Woloschak, G (2006) X-ray fluorescence microprobe imaging in biology and medicine. *Journal of Cellular Biochemistry* 99:1489–1502.
- Fahrni, C (2007) Biological applications of x-ray fluorescence microscopy: exploring the subcellular topography and speciation of transition metals. *Current Opinion in Chemical Biology* 11:121–127.
- Weiß, D et al. (2000) Computed tomography of cryogenic biological specimens based on x-ray microscopic images. *Ultramicroscopy* 84:185–197.
- Wang, Y, Jacobsen, C, Maser, J, Osanna, A (2000) Soft x-ray microscopy with a cryo STXM: II. Tomography. *Journal of Microscopy* 197:80–93.
- Schneider, G et al. (2002) Computed tomography of cryogenic cells. *Surface Review and Letters* 9:177–183.
- Larabell, C, Le Gros, M (2004) X-ray tomography generates 3-D reconstructions of the yeast, *Saccharomyces cerevisiae*, at 60-nm resolution. *Molecular Biology of the Cell* 15:957–962.
- Parkinson, D, McDermott, G, Etkin, L, Le Gros, M, Larabell, C (2008) Quantitative 3-d imaging of eukaryotic cells using soft x-ray tomography. *Journal of Structural Biology* 162:380–386.
- Berglund, M, Rymell, L, Peuker, M, Wilhein, T, Hertz, HM (2000) Compact water-window transmission x-ray microscopy. *Journal of Microscopy* 197:268–273.
- Tkachuk, A et al. (2007) X-ray computed tomography in Zernike phase contrast mode at 8 keV with 50-nm resolution using Cu rotating anode x-ray source. *Zeitschrift Kristallographie* 222:650–655.
- Kirz, J, Jacobsen, C (2009) The history and future of x-ray microscopy. *Journal of Physics: Conference Series* 186:012001.
- Chao, W, Harteneck, B, Liddle, J, Anderson, E, Attwood, D (2005) Soft x-ray microscopy at a spatial resolution better than 15 nm. *Nature* 435:1210–1213.
- Jefimovs, K et al. (2007) Zone-doubling technique to produce ultrahigh-resolution x-ray optics. *Physical Review Letters* 99:264801.
- Kang, H et al. (2008) Focusing of hard x-rays to 16 nanometers with a multilayer Laue lens. *Applied Physics Letters* 92:221114.
- Schneider, G (1998) Cryo x-ray microscopy with high spatial resolution in amplitude and phase contrast. *Ultramicroscopy* 75:85–104.
- Maser, J et al. (2000) Soft x-ray microscopy with a cryo STXM: I. Instrumentation, imaging, and spectroscopy. *Journal of Microscopy* 197:68–79.
- Wolter, H (1952) Spiegelsysteme streifenden Einfalls als abbildende Optiken für Röntgenstrahlen. *Annalen der Physik* 10:94–114, 286.
- Medalia, O et al. (2002) Macromolecular architecture in eukariotic cells visualized by cryoelectron tomography. *Science* 298:1209–1213.
- Fienuip, J (1978) Reconstruction of an object from the modulus of its Fourier transform. *Optics Letters* 3:27–29.
- Sayre, D (1980) in *Imaging Processes and Coherence in Physics*, Lecture Notes in Physics, eds Schlenker, M et al. (Springer-Verlag) Vol. 112, pp 229–235.
- Miao, J, Charalambous, P, Kirz, J, Sayre, D (1999) An extension of the methods of x-ray crystallography to allow imaging of micron-size non-crystalline specimens. *Nature* 400:342–344.
- Huang, X et al. (2009) Signal-to-noise and radiation exposure considerations in conventional and diffraction x-ray microscopy. *Optics Express* 17:13541–13553.
- Miao, J et al. (2002) High resolution 3D x-ray diffraction microscopy. *Physical Review Letters* 89:088303.

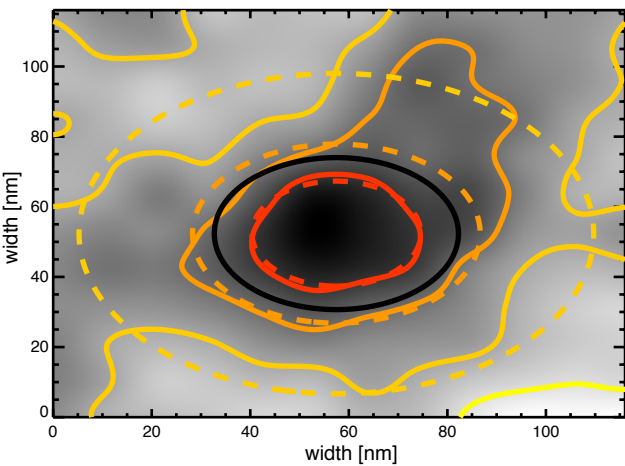
27. Chapman, H et al. (2006) High resolution ab initio three-dimensional x-ray diffraction microscopy. *Journal of the Optical Society of America A* 23:1179–1200.
28. Shen, Q, Bazarov, I, Thibault, P (2004) Diffractive imaging of nonperiodic materials with future coherent x-ray sources. *Journal of Synchrotron Radiation* 11:432–438.
29. Howells, M et al. (2009) An assessment of the resolution limitation due to radiation-damage in x-ray diffraction microscopy. *Journal of Electron Spectroscopy and Related Phenomena* 170:4–12.
30. Huang, X et al. (2009) Soft x-ray diffraction microscopy of a frozen hydrated yeast cell. *Physical Review Letters* 103:198101.
31. Lima, E et al. (2009) Cryogenic x-ray diffraction microscopy for biological samples. *Physical Review Letters* 103:198102.
32. Miao, J et al. (2003) Imaging whole escherichia coli bacteria by using single-particle x-ray diffraction. *Proceedings of the National Academy of Sciences* 100:110–112.
33. Shapiro, D et al. (2005) Biological imaging by soft x-ray diffraction microscopy. *Proceedings of the National Academy of Science* 102:15343–15346.
34. Jiang, H et al. (2008) Nanoscale imaging of mineral crystals inside biological composite materials using x-ray diffraction microscopy. *Physical Review Letters* 100:038103.
35. Song, C et al. (2008) Quantitative imaging of single, unstained viruses with coherent x rays. *Physical Review Letters* 101:158101.
36. Williams, G et al. (2008) High-resolution x-ray imaging of Plasmodium falciparum-infected red blood cells. *Cytometry Part A* 73A:949–957.
37. Nishino, Y, Takahashi, Y, Imamoto, N, Ishikawa, T, Maeshima, K (2009) Three-dimensional visualization of a human chromosome using coherent x-ray diffraction. *Physical Review Letters* 102:018101.
38. Spence, J, Weierstall, U, Howells, M (2002) Phase recovery and lensless imaging by iterative methods in optical, x-ray and electron diffraction. *Philosophical Transactions of the Royal Society of London A* 360:875–895.
39. Thibault, P, Elser, V, Jacobsen, C, Shapiro, D, Sayre, D (2006) Reconstruction of a yeast cell from x-ray diffraction data. *Acta Crystallographica A* 62:248–261.
40. Shapiro, D (2004) Ph.D. thesis (Department of Physics and Astronomy, Stony Brook University).
41. Schroer, CG et al. (2008) Coherent x-ray diffraction imaging with nanofocused illumination. *Physical Review Letters* 101:090801.
42. Raines, KS et al. (2010) Three-dimensional structure determination from a single view. *Nature* 463:214–217.
43. Rodenburg, J et al. (2007) Hard-x-ray lensless imaging of extended objects. *Physical Review Letters* 98:034801.
44. Thibault, P et al. (2008) High-resolution scanning x-ray diffraction microscopy. *Science* 321:379–382.
45. Jorgensen, P, Nishikawa, JL, Breikreutz, BJ, Tyers, M (2002) Systematic identification of pathways that couple cell growth and division in yeast. *Science* 297:395–400.
46. Tkacz, J, Barbara Cybulska, E, Lampen, J (1971) Specific staining of wall mannan in yeast cells with fluorescein-conjugated concanavalin a. *Journal of Bacteriology* 105:1–5.
47. Beetz, T et al. (2005) Apparatus for x-ray diffraction microscopy and tomography of cryo specimens. *Nuclear Instruments and Methods in Physics Research A* 545:459–468.
48. Marchesini, S et al. (2003) X-ray image reconstruction from a diffraction pattern alone. *Physical Review B* 68:140101.
49. Elser, V (2003) Phase retrieval by iterated projections. *Journal of the Optical Society of America A* 20:40–55.
50. Born, M, Wolf, E (1999) *Principles of Optics* (Cambridge University Press, Cambridge), Seventh edition.

Fig. 1. *Saccharomyces cerevisiae* yeast with the *whi5* mutation and labeled α -mannan as imaged using three methods: x-ray diffraction microscopy (XDM; a–c), scanning transmission x-ray microscopy (STXM; d), and scanning electron microscopy (SEM; e, f). For XDM, the reconstructed complex wave is represented using brightness for magnitude and hue for phase; three different focal planes are shown (obtained by Fresnel propagation from the plane of the tight support boundary (39)). The STXM image was acquired using a Fresnel zone plate with a 25 nm outermost zone width. For SEM, the specimen was manually flipped to obtain the front and back views shown. The back view was inverted for easier comparison. Different tilts produce the apparent distortion between the two images. (a) Two vacuoles (V) are shown (bright yellow), along with structures which may be a mitochondrion (M) and the nucleus (N) of the upper right cell. The image agrees well with the STXM image (d), though the STXM image field does not contain the entire upper right cell. The two cells are smaller than the typical size expected of the *whi5* mutation, which indicates that the cells may have shrunk from radiation delivered before diffraction data was recorded (40). (b and e) Comparison between immunogold labels (indicated with arrows) visible on the electron-beam-facing surface of the cells using SEM (e) and at an equivalent focal plane using XDM (b). The labels on the thicker areas of the specimen are less visible in the XDM image. (c and f) Comparison between immunogold labels visible on the opposite surface of the cells using SEM (f) and the equivalent focal plane using XDM (c). The red arrow indicates the specific label discussed in Fig. 2. Boxed areas of interest in the three x-ray micrographs are shown at 2 \times magnification, with color levels scaled to show better contrast.

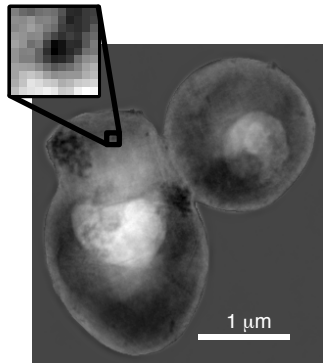
Fig. 2. Estimation of image resolution based on a view of a single silver-enhanced gold label indicated with a red arrow in Fig. 1e. The magnitude of the XDM wavefield of Fig. 1 is shown at right. A subfield of this image centered on the label of interest was extracted as indicated by the box, and cubic interpolation was then used to expand the image from an original pixel size of 10.6 nm to a pixel size of 0.53 nm. This expanded subfield is shown at left, along with solid isomagnitude contour lines (yellow hues indicate contours of higher magnitudes). It was then fit to a 2D Gaussian, with the result of a full width at half maximum (FWHM) major diameter of 51.2 nm (horizontal in this view) and 44.8 nm minor diameter. The radius of this gold label was estimated from the SEM image of Fig. 1e to be 31.9 nm \pm 2.5 nm. Convolution of the thickness function of a 32 nm radius sphere with Gaussian point spread functions of various widths, we arrive at a real-space resolution estimate in the 10–20 nm range.

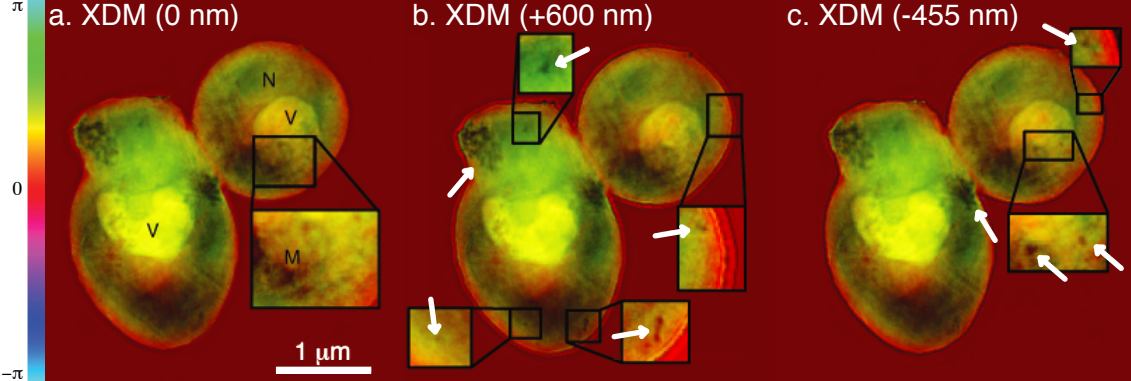
Fig. 3. The phase retrieval transfer function (PRTF; defined as the ratio of the averaged reconstructed Fourier magnitudes to the recorded magnitudes) provides a measure of reproducibility of diffraction phasing as a function of resolution length scales. The PRTF for the reconstructed image of Fig. 1a is shown. The function is relatively flat until a spatial frequency of about 40 μm^{-1} , corresponding to a half-period resolution of 12.5 nm where it begins to decline. At the real space pixel size of 10.6 nm, indicated by the vertical dashed line, the PRTF value remains above 0.4.

Fig. 4. Three independently reconstructed x-ray micrographs at -30° , 0° , $+15^\circ$ tilt angles. Magnitude is shown as brightness and phase as hue. The two vacuoles (V) and the upper right nucleus (N) are shown.

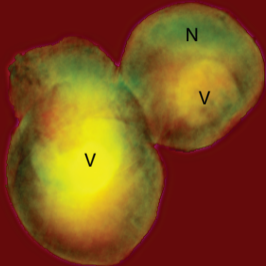


— Interpolated pixels
- - Gaussian fit
■ FWHM

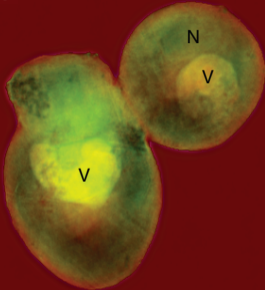




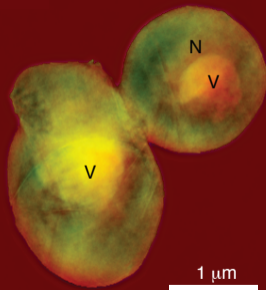
-30°



0°



+15°



1 μ m



